Compressed sensing of human breast optical coherence 3-D image volume data using predictive coding

Diego M. Song Cho,[1] 🔘 **Manuel J. Jerome,[2] and Christine P. Hendon[2],***

[1]*Department of Biomedical Engineering, Columbia University, 500 W 120th Street, New York, NY 10027, USA*

[2]*Department of Electrical Engineering, Columbia University, 500 W 120th Street, New York, NY 10027, USA*

*cpf2115@columbia.edu

Abstract: There are clinical needs for optical coherence tomography (OCT) of large areas within a short period of time, such as imaging resected breast tissue for the evaluation of cancer. We report on the use of denoising predictive coding (DN-PC), a novel compressed sensing (CS) algorithm for reconstruction of OCT volumes of human normal breast and breast cancer tissue. The DN-PC algorithm has been rewritten to allow for computational parallelization and efficient memory transfer, resulting in a net reduction of computation time by a factor of 20. We compress image volumes at decreasing A-line sampling rates to evaluate a relation between reconstruction behavior and image features of breast tissue.

1. Introduction

Breast cancer is the second most common cancer in women in the United States [1]. There has been increased interest in using high-resolution imaging modalities for evaluating breast tissue in real-time. OCT is being studied for use in breast cancer diagnostics and disease progression tracking [2–9]. Histology remains the gold standard for tissue evaluation, but its processing is both costly and time-consuming. OCT has been shown to be able to identify normal breast parenchyma as well as pathologic conditions such as ductal carcinoma *in situ* (DCIS), invasive ductal carcinoma (IDC), and microcalcifications [9–11]. Ultrahigh resolution OCT has shown strong histological correlations [9] to aid manual diagnosis of pathological conditions of the breast. In addition, functional extensions of OCT, such as optical coherence elastography [4,12] and polarization-sensitive OCT [13,14], and alternatives, such as Raman spectroscopy [15–17], have been investigated.

　Optical coherence tomography (OCT) is capable of acquiring 3-D images at micron resolution over a large field-of-view. Typical OCT image volumes can contain hundreds of millions of pixels. Optimally, imaging modalities used in the clinical setting will have a large field of view and a high spatial resolution. With these two criteria prescribed, the minimum scan acquisition time is fixed by the amount of data that must be acquired. Normally, this amount of data is dictated by the Nyquist-Shannon sampling theorem [18,19]. Given the fact that resected breast tissue is typically larger than the standard OCT field of view (4 mm), there is a need to use a form of OCT that can image large areas within a short period of time, thus requiring large image scales. Based on the Nyquist-Shannon sampling theorem, a large number of non-redundant samples must be obtained for all bandlimited signals – in the case of spectral domain OCT, the measurements are taken in the Fourier domain. Under conventional reconstruction, the total number of samples required in the Fourier domain is determined by the spectral range of the spectrometer and the imaging depth required [20]. This in turn results in a high sampling rate for images requiring

large imaging depth and high axial resolution. Overall, this poses a heavy burden for acquisition, processing, and storage.

In this paper, we thus propose the use of compressed sensing to decrease the rate of OCT data sampling, thus reducing the amount of data required while maintaining fidelity in high-resolution image reconstruction. Recent developments in applied mathematics have demonstrated that application of the theory of compressed sensing is a promising approach in reducing scan acquisition times by sub-sampling below the Nyquist rate, provided that the target image is sparse [21]. The compressed sensing technique can provide high spatial resolution while vastly reducing the number of samples required for acquisition. Therefore, the total scan acquisition time, which is a crucial aspect to consider in the clinical setting, can be minimized.

1.1. Compressed sensing

Compressed sensing (CS) is a technique that enables the reconstruction of images from highly-undersampled data, provided that the signal is sparse in some representation basis [21]. This allows acquisition of data at sub-Nyquist rates and reconstruction that results in images with quality close to the ground truth or at the maximum possible resolution.

CS has already had notable successes when applied to several medical imaging modalities, such as magnetic resonance imaging (MRI) [22–24], computed tomography (CT) [25], diffuse optical tomography [26,27], and photoacoustic imaging [28–32]. Applications of CS in OCT imaging have been reported by many groups [20,33–35] and high quality imaging has been obtained with a significantly reduced amount of measurements compared to the Nyquist rate requirement. Applying compressed sensing to OCT can enable faster acquisition while preserving image quality. Considering that OCT images are volumetric 3-D scans, compressed sensing offers the possibility of undersampling across one, two, or all three dimensions of acquisition. Several groups [20,36] have performed simulations of compressed sensing along the A-line scan axis (spectral sub-sampling) to reduce hardware complexity (lesser number of pixels). Duflot et al. [37] have performed sub-sampling across the *en face* plane and recovered full images based on sparsity in the Shearlet transform.

Based on the observation that denoised, difference images of adjacent OCT B-scans are sparse in the Fourier basis, our group has proposed the Denoising Predictive Coding (DN-PC) compressed sensing algorithm for recovering undersampled volumetric OCT data [38]. We evaluated the effectiveness of DN-PC using simulations on synthetic subsamples taken from full-resolution images, and compared the recovered results with a reference. DN-PC demonstrated improved performance over other known compressed sensing algorithms on a variety of clinically relevant datasets, and as expected, there has been a net reduction of data size upon compression.

1.2. Study goals

Though 3-D OCT has shown potential for real-time breast tissue evaluation and cancer diagnosis, in standard Nyquist-based usage, it requires a long data acquisition time and a large amount of spectral measurements, making it susceptible to motion artifacts and to clinical workflow constraints that do not allow for lengthy operations. Furthermore, given the large size of breast tissue samples (an average specimen size is $1.2\,cm^2$, and typically has a range between 1.0 and $4.0\,cm^2$), OCT procedures in clinical settings may often require undersampling to achieve coverage of large fields of view.

The introduction of DN-PC has laid important groundwork for developing a CS-OCT solution that could be generalized to reconstruct and analyze any tissue type [38]. However, as OCT systems become more sophisticated and achieve higher resolutions, reconstruction methods may face higher degrees of error as tissue features to reconstruct appear to be smaller and more finely detailed. This study therefore aims to address the higher reconstruction error shown for breast tissue data over other tissue types, to further understand the relation between CS-based

reconstruction behavior and features of finely-detailed tissue, such as breast adipose. We aim to apply DN-PC for compression of volumes at various sampling rates to evaluate this relation. In doing so, we also work to improve the algorithm's computational performance to demonstrate that it has promise in its utility. The study analyzes the impact of compressed sensing-based reconstruction on image texture feature preservation. In addition, we compare our reconstruction to standard methods used to address image acquisition speed and downsampling.

2.　Methods

2.1.　Imaging protocol

Breast tissue specimens used consisted of discarded tissue that was not required for diagnosis as defined by the Department of Pathology at the Columbia University Medical Center (CUMC). Specimens were collected from 49 patients undergoing surgical procedures. They consisted of normal tissue from breast reductions and tumor samples from mastectomies. The protocol was considered as non-human subject research in accordance with 45CFR46 and was performed under Columbia University Tissue Bank IRB AAAB2667. All tissue samples were de-identified. Specimens were imaged *ex vivo* within 24 hours after excision. Imaging was performed with a home-built ultrahigh resolution (UHR) spectral-domain OCT system, with an optical window of 800 nm, an axial resolution of 2.7 μm, and a lateral resolution of 5.5 μm (in air). Volumes were acquired at 32 kHz linerate, and images measured 800 by 1024 pixels, which physically correspond to 3.0 mm by 1.78 mm, respectively [6].

2.2.　Compressed sensing algorithm

The DN-PC algorithm used within this paper was adopted from a prior study published by our group [38]. Briefly, the problem of recovering full samples, X, from sub-samples, contained in A, can be written in the matrix form: $A = DX$, where D is the sub-sampling matrix mapping from X to A. The linear equation on its own is under-determined, but if X is sparse in some basis, compressed sensing can be applied to recover solutions with probability of arriving at the correct solution correlated to the level of sparsity.

　　Let Ψ be the combination of a regularization term and the transform in which X is sparse, then the compressed sensing method can be written as solving the optimization problem $argmin(X)$ for $f(x) = ||A - DX||_2 + |\Psi(X)|_1$. Since the problem does not have a closed form solution, it requires the use of iterative solvers. The choice of Ψ affects the convexity and differentiability properties of the objective function and hence influences the possible choices of iterative solvers.

　　Ψ is a Gaussian blur (of a size to-be-determined) followed by a Fourier transform. For the objective function, the absolute value after the Fourier transform is used to compute the ℓ_1 norm. In summary, the DN-PC solver uses a combination of iterative shrinkage thresholding and proximal gradients to both recover the image and also decide the optimal blur size to be used. The solver converges to a solution if the sparsity holds, else it fails to converge should the sparsity condition be insufficient. Within this paper, we explore the impact of the DN-PC algorithm within OCT images of human breast tissue, which has heterogeneous tissue architecture.

2.3.　Parallelization

Previous work has shown reconstruction times of over 10 hours [38] for a 100 B-scan volume (800 x 512 pixels per B-scan) using a CS reconstruction algorithm combining a TVL1 reconstruction method by Yang et al. [39] and a predictive coding approach. This was further improved upon with the DN-PC algorithm at 19 minutes for reconstruction of the same volume [38]. However, to ensure feasibility of imaging within a clinical environment, the reconstruction times need to be faster. The computationally intensive operations involved in DN-PC, namely 2-D convolution

and 2-D Fourier transform, can be made faster using parallel processing, and the intermediate norm computations can also be optimized.

The code was rewritten to enable parallel processing improvements by leveraging the MATLAB Parallel Processing Toolbox and NVIDIA CUDA backend functions, which have GPU-optimized expressions for computing 2-D Fourier and inverse Fourier transforms, Gaussian filtering, Frobenius norm, element-wise addition, multiplication, division, and absolute magnitude operations. The rewrite was necessary to enable batching, vectorization, memory coalescing, and efficient memory transfers between the CPU and GPU and to optimize other complex operations into GPU/SIMD-optimized, divergence-free conditional operations in native MATLAB array syntax. All the processing is done inside the GPU, and only the final results are returned to the CPU by using a `gather` operation.

The core algorithm after the rewrite remained mathematically equivalent to that of McLean et al. [38], and all other hyperparameters, with the exception of patch size and maximum permissible of iterations for convergence ($\mathcal{I}$), were unmodified. To ensure that there was no bottleneck in memory transfers, the patch size was required to be at least 256 x 256 pixels for the system performing the computations. The new maximum number of iterations was increased to 100 for the first B-scan and remained fixed to the default 20 for subsequent scans.

The batching involves slicing the subsampled images and their corresponding subsampling matrix into patch-sized blocks to be processed. In the original implementation of DN-PC, the iterative solver has a conditional division, which divides by α at the predicted points, or by $(1 + \alpha)$ at subsampled points, where α is a rough measure of noise (see Equation 7 in [38]). In the newly parallelized implementation, this expression is instead vectorized as a parallelized, element-wise division. This is achieved by pre-computing a matrix of element-wise divisors that are mapped from the subsampling matrix.

The entire batched data is pre-loaded into the GPU. The algorithm processes all patches comprising a B-scan and then iterates to the next B-scan. Given that adjacent B-scans are similar, it is efficient to store the previous B-scan's reconstruction results (on the GPU) and use these as initial values for the next iteration. In our implementation, 2-D FFT and Gaussian filtering is written into a single line of code by composing their respective MATLAB functions (`imgaussfilt` and `fft2`). MATLAB performs the operations separately: `imgaussfilt` followed by `fft2`.

The parallel processing improvements are applicable to any systems with a modern X86 CPU, with optional multi-threading, and CUDA-enabled GPUs.

2.4. Study parameters

A custom selection of 104 volumes, representative of three breast tissue subtypes (36 volumes of adipose, 35 of stroma, 33 of cancer), was compiled for image reconstruction using the DN-PC algorithm. Volumes of 100 B-scan OCT images for each breast tissue specimen were used for reconstruction. The dataset was derived from the data collected previously by our group [6]. The following parameters were used: $\alpha = 0.1$, $\beta = 1$, $\lambda_{max} = [3, 4]$, $\lambda_{min} = [0.2, 0.4]$, $\mathcal{J} = 20$, $\mathcal{I} = 20$, convergence threshold $\tau = 10^{-3}$, with staggered sampling and periodic full-resolution acquisitions every 10 consecutive frames ($\mathcal{I}_b = 10$).

Compression was done at various A-line sampling rates (50%, 25%, 10%, 5%, 2.5%, 1%). The compression and image reconstruction using DN-PC was done using a Windows 10 desktop with an Intel Core i9-9900K CPU at 3.6 GHz, a NVIDIA GeForce RTX 2080 GPU, and 128 GB of RAM. The algorithm was fully run on MATLAB 2021b.

2.5. Metrics

Several quantitative metrics were selected to assess and compare compressed sensing reconstruction performance. The first measure is Relative Error, which measures the intensity difference

between the original and reconstructed images. It is defined as

$$\text{Relative Error} = \frac{||x_{\text{recon}} - x||_F}{||x||_F} \tag{1}$$

where x is the original OCT volume and x_{recon} is the reconstructed volume. The norm utilized in the Relative Error measure is the Frobenius norm instead of the standard ℓ_2 norm.

The second measure is the Structural Similarity Index Measure (SSIM), which evaluates the similarity between two images using luminance, contrast, and structure as quantitative elements (Eq. (2)) [40]. The SSIM is a value between 0 and 1, where a value of 1 indicates that the evaluated images are identical, and 0 indicates otherwise. Mathematically, SSIM is defined as follows,

$$\text{SSIM}(x, y) = \frac{(2\mu_x\mu_y + C_1)(2\sigma_{xy} + C_2)}{(\mu_x^2 + \mu_y^2 + C_1)(\sigma_x^2 + \sigma_y^2 + C_2)} \tag{2}$$

where $\mu_x, \mu_y, \sigma_x, \sigma_y$, and σ_{xy} are the local means, standard deviations, and cross-covariance for images x and y. C_1 and C_2 are the regularization constants for luminance and contrast, respectively.

All cases involved a 3×3 pixel median filter for denoising, applied to both the ground truth and the reconstructed volumes before measuring performance metrics such as relative error and SSIM.

2.6. Texture features comparison between CS and classic reconstruction

Previous studies have shown that texture features are different between normal fibrous stroma, cancer, and adipose tissue [6,41,42]. Therefore, we first evaluated if images reconstructed using the DN-PC algorithm altered texture features. In addition, a standard method to reduce net acquisition time is by undersampling the target image. Downsampled images can then be upscaled in size to the desired resolution, and missing information in pixels is added by interpolation. To compare the performance of image reconstruction between the compressed sensing algorithm and this classic form of downsampling and interpolation, select images from each tissue type (adipose, normal stroma, and cancer) were chosen. Original images from OCT volumes were decimated to the same sampling rates as the ones performed with the DN-PC algorithm. The downsampled images were then upsampled using an implementation of the `interp2` built-in function in MATLAB.

Quantitative texture features were extracted from CS-reconstructed images and classic downsampling and interpolated OCT images. In each OCT image, texture features were extracted from a Grey Level Co-occurrence Matrix (GLCM) implemented using the `graycomatrix` built-in function in MATLAB. Since its invention, GLCM has played a vital role in many texture-based image analysis applications [43,44], and also serves well in the selection of features to be used as inputs for machine-learning classification algorithms [42,45]. Selected features included Entropy, Skewness, Dissimilarity, Maximum Probability, GLCM Mean, GLCM Variance, Contrast, Energy, Correlation, and Homogeneity. Feature extraction was performed in hand-selected regions of interest (ROI) from the B-scans with each ROI having a size of 160-by-160 pixels and spanning a region containing the designated tissue type (see Figure 1).

Analysis was also performed to assess preservation of optical parameters. We calculated the mean attenuation coefficient for a 40-by-40 pixel ROI automatically placed within tissue in one B-scan sample per available cancer ($n = 28$) and stroma ($n = 34$) volumes.

Statistical differences between the groups were examined using a one-way analysis of variance (ANOVA), followed by a Tukey multiple comparisons test. Statistical calculations were done using GraphPad Prism 9.
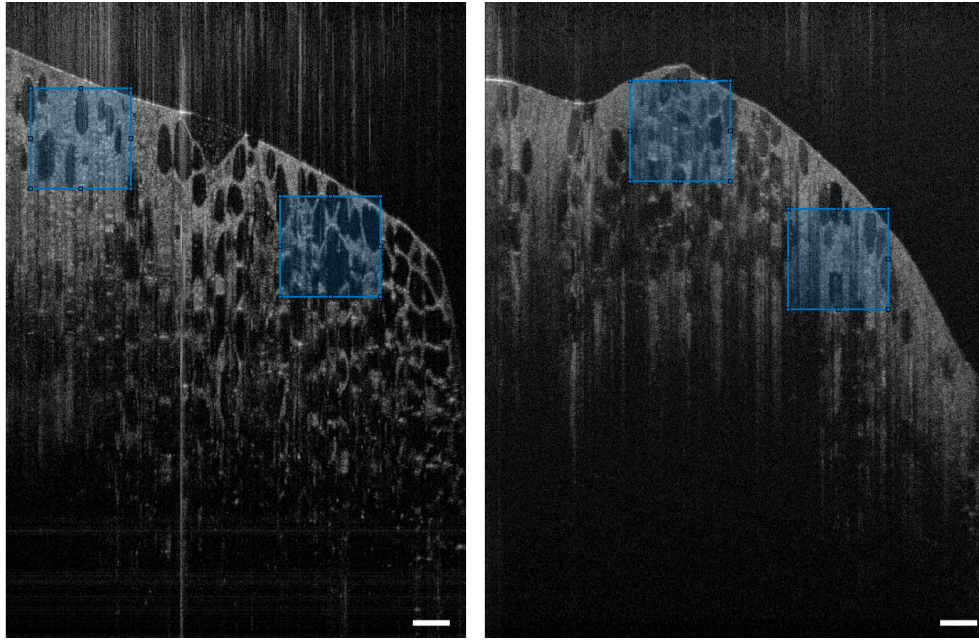
Fig. 1. Selection of regions of interest (ROIs, blue) for feature extraction and texture analysis (scale bar = 250 *μm*).

3.   Results and discussion

3.1.   Compressed sensing of breast OCT volumes - overall performance

The DN-PC algorithm was applied with varying levels of undersampling (50%, 25%, 10%, 5%, 2.5%, and 1% of total samples). Image reconstructions were separated by tissue types shown in breast tissue samples: normal adipose, normal stroma, and cancerous tissue. Across all levels of compression, high-level features appear to be preserved in tissue, particularly over stroma and cancer specimens, and in a majority of adipose tissue samples. Qualitatively (Figure 2), images at 50% sampling appear nearly identical to the full-resolution B-scans. 25% and 10% samples demonstrate a small introduction of noise, and fine features become blurred with minor vertical streaking. At higher levels of compression, particularly in images of adipose, walls and edges appear distorted. In some cases, there is a notable amount of morphological opening, especially in globular sections of the adipose, and in empty spaces within normal stroma or cancer tissue (see arrows in Figure 2). Due to the patch-based nature of the reconstruction algorithm, square-shaped artifacts appear as compression becomes more stringent (beginning at 10%) at varying intensities, spanning entire images and displaying separation of intensity levels between adjacent patches. This effect is more prominently displayed in images of adipose, but present in all cases (shown by arrows in Figure 2).

Quantitative metrics included relative error and structural similarity index, whose increasing and decreasing trends, respectively, are reported in Figure 3 and on Table 1. Relative error for reconstruction had a range of 14% to 34%. Significant differences are present among 50%, 25%, and 10% sampling rates, but then changes become unsubstantial for more stringent sampling conditions. There is an overall increasing trend in relative error as the degree of compression increases. Simultaneously, there is a monotonically decreasing relation for structural similarity as undersampling is more severe. Median SSIM values generally ranged from 37% to 75% in degree of similarity between original and reconstructed image volumes. Like relative error, major
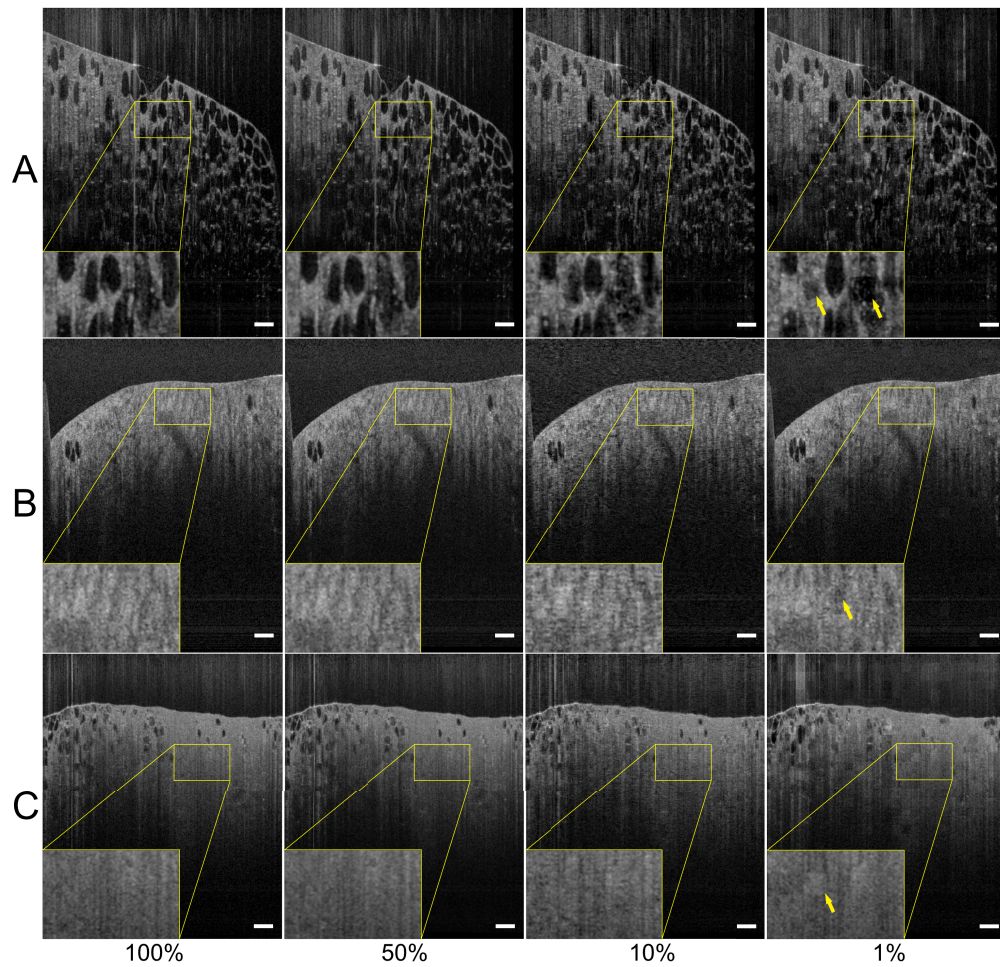
Fig. 2. Breast tissue DN-PC based image reconstructions by tissue subtype (A = normal adipose, B = normal stroma, C = cancer) at four A-line sampling rates (scale bar = 250 μm). Zoomed-in subregions are depicted (bottom left) for each frame; arrows indicate morphological changes and patch-shaped artifacts that appear as compression is higher.

differences in SSIM occurred down to 10% sampling rate, but became marginal or insignificant for more stringent sampling conditions. The denoised results appear improved over raw data results across all cases.
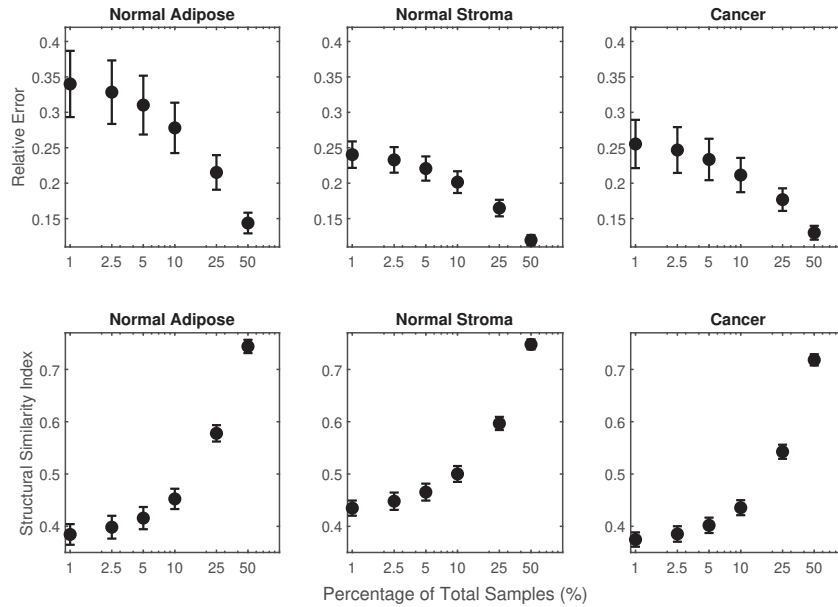

Fig. 3. Relative error and structural similarity analysis. (Reported values are medians and 95% confidence intervals, with $n = 30, 28, 34$ numbers of measurements, respectively)

Figure 3 demonstrates how relative error and structural similarity index measure (SSIM) decrease and increase respectively, as the percentage of samples increases towards the totality (100%) of samples.

While there is no observable correlation for computation time in relation to sampling rate, the implementation of parallel processing greatly reduced net computation time by over at least twenty-fold, as shown in Table 1. Computation time decreased significantly compared to the pre-parallelized implementation of DN-PC, from an average reconstruction time of 60 minutes to under 2 minutes for the same 100 B-scan volume. This improvement in computation time is achieved thanks to the parallel processing algorithm re-write. Batch size was also increased significantly from the first implementation of DN-PC [38], from a 32-by-32 pixel patch size, to 256-by-256 pixels on the current implementation. DN-PC applied with a larger patch size and the parallel processing method yielded better results, with the edge distortions and streaking artifacts significantly reduced. In both cases of small and large patch sizes, there was no observable correlation for computation time in relation to sampling rate.

3.2. Texture features comparison between CS and classic reconstruction

As shown in Fig. 1, two 160-by-160 pixel ROIs were selected by hand from two select B-scan examples for each tissue type, so that texture features based on a grey-level co-occurrence matrix could be extracted for quantitative comparison between compressed sensing-based image reconstruction and traditional downsampling-and-interpolation-based reconstruction.

An important underpinning of using novel techniques, such as DN-PC, is that they must perform equally or better than classical or existing state-of-the-art methods. Overall, at the expense of algorithmic complexity, DN-PC is shown to be able to preserve grey-level texture features when compared to classically downsampled and interpolated images.

Table 1. Quantitative summary of computation time, relative error and structural similarity of breast OCT image reconstructions using DN-PC for normal adipose, normal stroma, and cancer at A-line sampling rates of 50%, 25%, 10%, 5%, 2.5%, and 1%. Values are reported before and after parallelization of the algorithm. Reported quantities are median values.

Tissue	Not Parallelized			Parallelized		
	Computation Time (s)	Relative Error	SSIM	Computation Time (s)	Relative Error	SSIM
Adipose						
50%	3040.5	0.1766	0.7162	95.1	0.1438	0.7439
25%	3983.5	0.2342	0.5873	85.2	0.2152	0.5778
10%	5075.3	0.2989	0.4715	97.3	0.2780	0.4525
5%	3630.5	0.3329	0.4399	90.6	0.3102	0.4158
2.5%	2195.6	0.3569	0.4301	92.0	0.3285	0.3984
1%	3660.6	0.3569	0.4301	97.7	0.3401	0.3845
Stroma						
50%	2984.9	0.1256	0.6971	98.2	0.1195	0.7183
25%	4125.2	0.1754	0.5534	93.9	0.1649	0.5426
10%	5781.7	0.2203	0.4440	100.4	0.2015	0.4356
5%	5421.8	0.2377	0.4098	94.6	0.2207	0.4019
2.5%	2612.4	0.2499	0.3964	95.7	0.2329	0.3854
1%	2967.9	0.2499	0.3964	99.2	0.2403	0.3748
Cancer						
50%	3392.7	0.1451	0.7128	96.7	0.1301	0.7478
25%	3568.2	0.1947	0.5935	91.5	0.1768	0.5967
10%	3977.8	0.2259	0.5046	97.9	0.2115	0.5001
5%	3751.5	0.2483	0.4781	92.7	0.2335	0.4655
2.5%	2389.9	0.2631	0.4671	93.1	0.2468	0.4481
1%	1992.4	0.2631	0.4671	98.0	0.2553	0.4348

Figures 4, 5, and 6 depict statistical differences between groups calculated from a one-way ANOVA and Tukey multiple comparisons. The figures show that for more constrained levels of classic interpolation, texture features lose information to compression and show statistically significant ($p < 0.05$) differences. In contrast, the CS-OCT-based method manages to preserve texture features relative to the original image, for nearly every GLCM-based feature investigated. Across the three tissue types, GLCM mean, kurtosis, and skewness do not appear to vary significantly for both the compressed sensing and the classic downsampling and interpolation cases, whereas the largest changes are apparent in features such as contrast, correlation, and dissimilarity, all of which are measures of difference or distinction of some sort.

Further analysis was performed to assess whether the compressed sensing approach conserves optical parameters, the attenuation coefficient being of particular importance. No statistically significant difference ($p < 0.05$) was found among most comparisons between the original and the CS-OCT-based samples (50% to 1% for cancer and 50% to 5% for stroma). This is consistent with the finding that texture features also appear to be preserved across CS-based reconstructions.
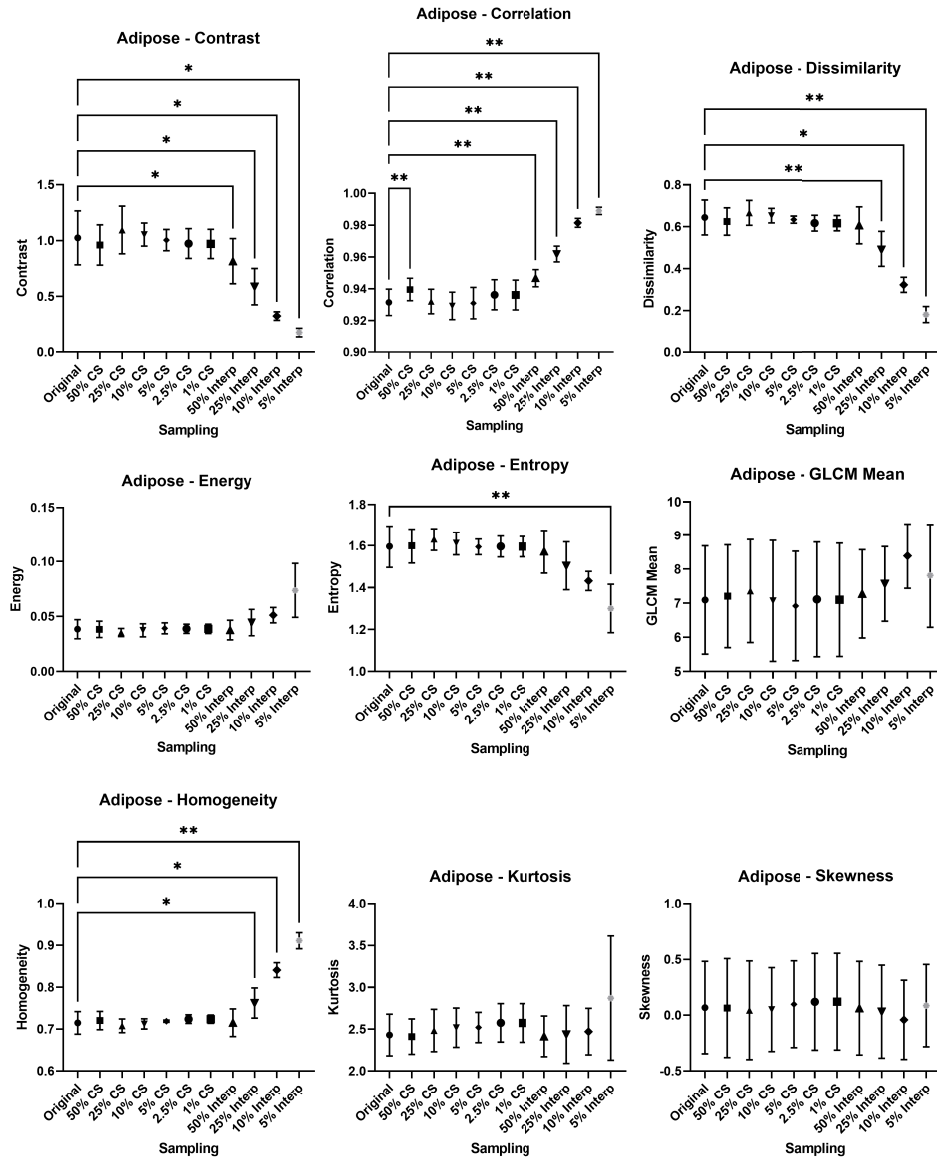
Fig. 4. Statistical analysis of nine GLCM-based texture features for adipose tissue, from the original image, the CS-based image reconstruction at varying degrees of compression, and traditional, interpolated images at varying rates. Statistical significance reported by p-value (* $p < 0.05$, ** $p < 0.01$, *** $p < 0.001$). Values are reported as means +/- S.D. over 4 ROI selections.
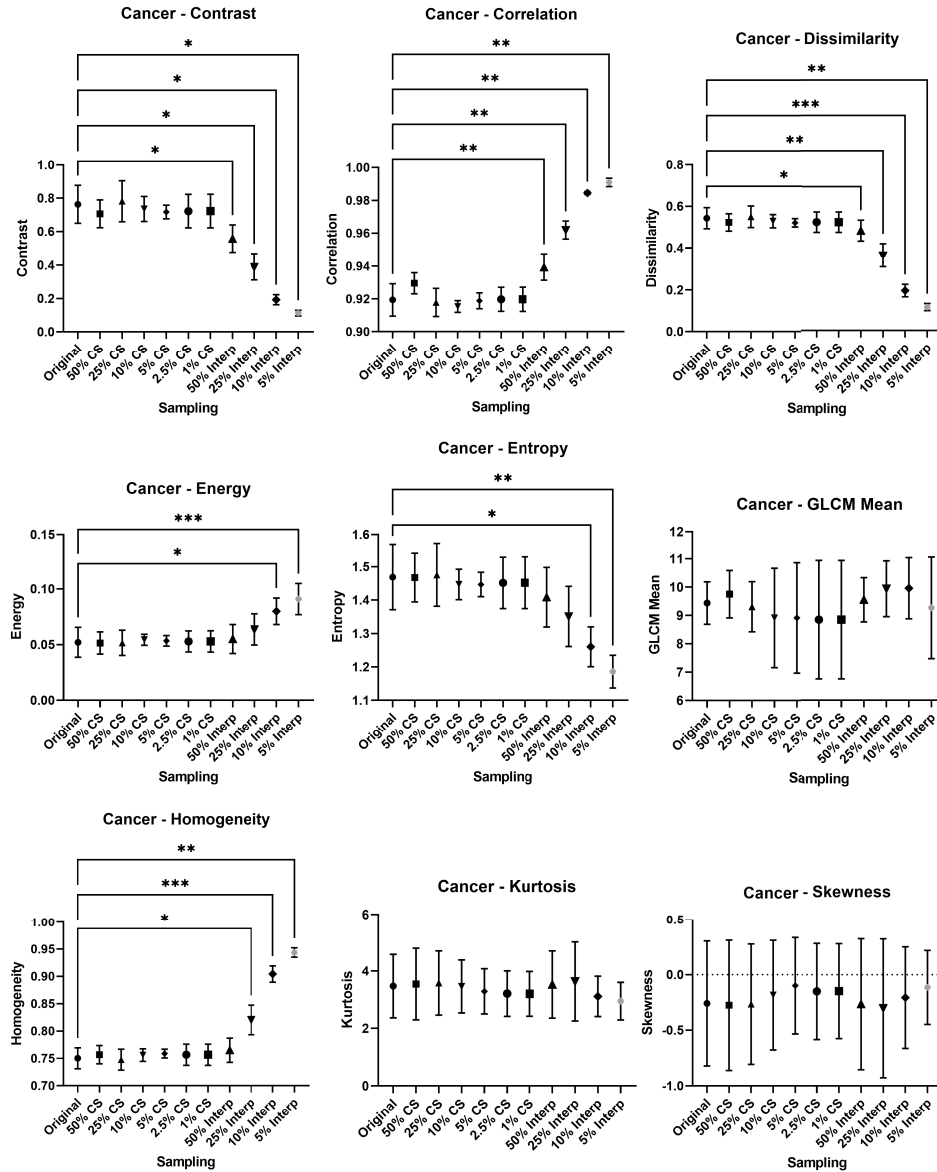
Fig. 5. Statistical analysis of nine GLCM-based texture features for cancerous breast tissue, from the original image, the CS-based image reconstruction at varying degrees of compression, and traditional, interpolated images at varying rates. Statistical significance reported by p-value (* p < 0.05, ** p < 0.01, *** p < 0.001). Values are reported as means +/- S.D. over 4 ROI selections.
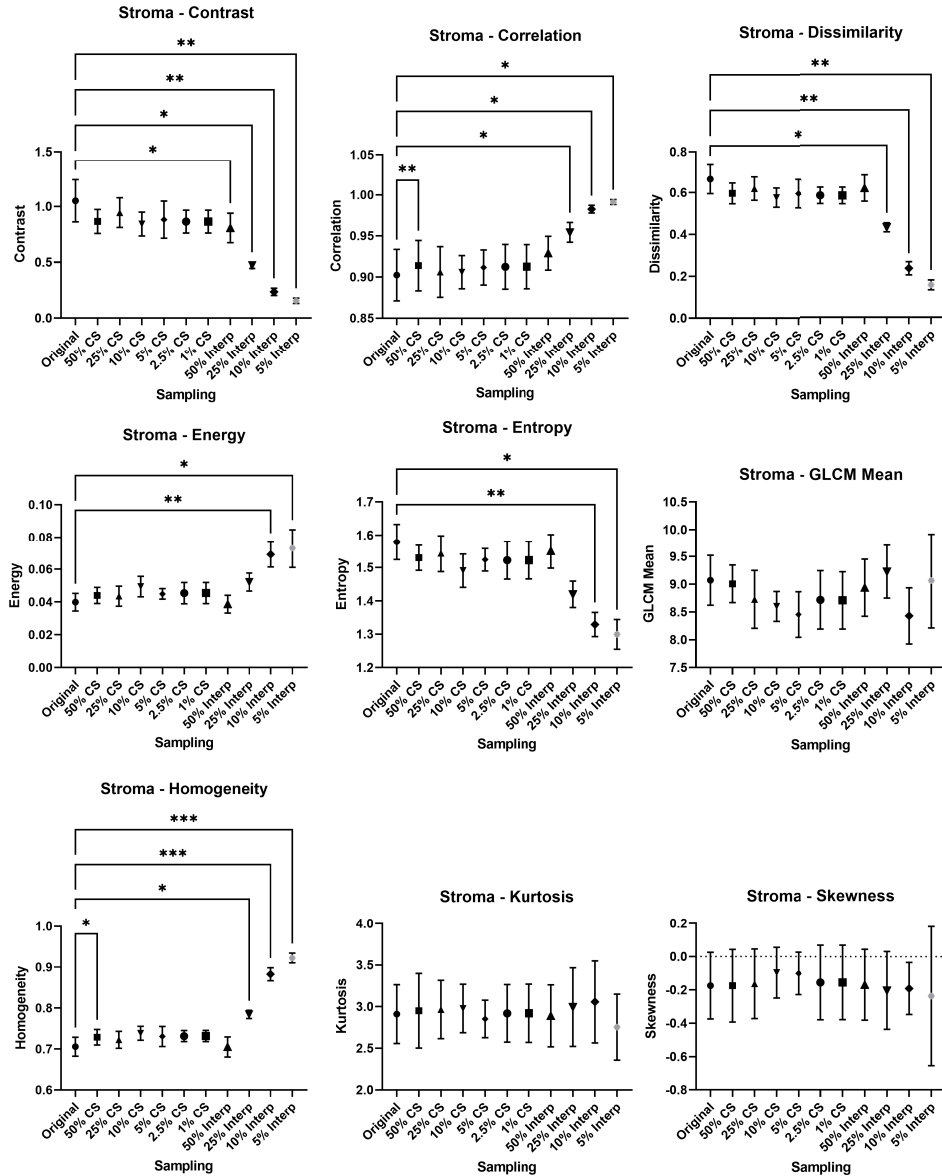
Fig. 6. Statistical analysis of nine GLCM-based texture features for normal stroma of breast tissue, from the original image, the CS-based image reconstruction at varying degrees of compression, and traditional, interpolated images at varying rates. Statistical significance reported by p-value (* p < 0.05, ** p < 0.01, *** p < 0.001). Values are reported as means +/- S.D. over 4 ROI selections.

3.3.   Limitations and future work

With regards to tissue type, it is apparent that CS-OCT reconstruction of breast adipose tissue is more challenging than that of cancerous or normal stroma of breast tissue. This qualitative difference may be attributed to the presence of porous structures that do not conform well to the sparsity conditions required by compressed sensing. The results with DN-PC, while much better than classical downsampling, have room for improvement, as the algorithm's iterator appeared to fail in converging and producing images closer to the original, full-resolution images. Though resulting images appeared visually similar, we suspect this similarity is due to how tissue structure remains similar across adjacent volume slices, so this overall structure is preserved nonetheless. We also note that the apparent size of adipose globules may appear independent of the convergence of the iterator, as size appears to change regardless of convergence.

The choice of full-slice sampling distance, which is defined by the parameter $\mathcal{I}_b$ and involves periodically preserving a full-resolution scan to "reset" any remaining propagated error [38], appeared to introduce height variations that appeared across slices, and hence the sparsity of the difference image was affected. In our dataset, there is a sharp decline in reconstruction accuracy when choosing to preserve a full-resolution scan every 20 or more slices. Hence, the full-slice sampling distance was set to every 10 slices. Image registration by slice in OCT volumes prior to image reconstruction can be a focus of future research and may allow even smaller effective sub-sampling ratios.

We employed the structural similarity index metric to analyze the performance of the DN-PC algorithm in reconstructing tissue structures. It is a refined metric that also accounts for perceptual masking phenomena [46], and can show the effectiveness of the compressed sensing algorithm over the other interpolation methods. However, when observing the metric across slices in single volumes, we noticed that the DN-PC reconstructed images appeared qualitatively and visually more similar to one another than the calculated SSIM implied. In other words, we observed that the accumulation of error that propagated between periodically sampled full-resolution slices accounted for a sharp decline in the SSIM. But qualitatively, image quality did not appear to deteriorate as sharply as the decline in SSIM seemed to indicate. It may be appropriate for future research to consider other quantitative metrics to discern the performance of image reconstruction on different levels, such as a per-slice level and a per-volume level.

Although classification performance was not assessed in this study due to small sample size, future research could involve the combination of hardware-based CS-OCT implementation and diagnostic-focused classification.

4.   Conclusion

Compressed sensing provides overall improvements in image reconstruction, opening up the possibility of revision in current optical hardware, and higher efficiency in OCT-based image acquisition for clinical workflow. Our work proves a remarkable improvement in image reconstruction speed given undersampled data while preserving image quality and features to a great extent. CS-OCT has the potential to significantly alter the presently established clinical workflow for breast cancer assessment, by introducing OCT as a means of rapid intraoperative assessment in place of frozen section analysis and pathology studies. Coupled with automated image analysis, implementation of compressed sensing could also reduce the need for re-excision of tumors by allowing rapid assessment of cancer margins, thus improving diagnostic speed relative to standard histological procedure and boosting diagnostic accuracy.

Disclosures. The authors declare no conflicts of interest related to this article.

Data availability. Data underlying the results presented in this paper are not publicly available at this time but may be obtained from the authors upon reasonable request.

References

1. N. Howlader, A. M. Noone, M. Krapcho, J. Garshell, N. Neyman, S. F. Altekruse, C. L. Kosary, M. Yu, J. Ruhl, Z. Tatalovich, H. Cho, A. Mariotto, D. R. Lewis, H. S. Chen, E. J. Feuer, and K. A. Cronin, "Seer cancer statistics review, 1975-2010," National Cancer Inst. (2013).
2. W. Luo, F. T. Nguyen, A. M. Zysk, T. S. Ralston, J. Brockenbrough, D. L. Marks, A. L. Oldenburg, and S. A. Boppart, "Optical biopsy of lymph node morphology using optical coherence tomography," Technol. Cancer Res. Treat. **4**(5), 539–547 (2005).
3. F. T. Nguyen, A. M. Zysk, E. J. Chaney, J. G. Kotynek, U. J. Oliphant, F. J. Bellafiore, K. M. Rowland, P. A. Johnson, and S. A. Boppart, "Intraoperative evaluation of breast tumor margins with optical coherence tomography," Cancer Res **69**(22), 8790–8796 (2009).
4. K. Kennedy, R. McLaughlin, B. Kennedy, A. Tien, B. Latham, C. Saunders, and D. Sampson, "Needle optical coherence elastography for the measurement of microscale mechanical contrast deep within human breast tissues," J. Biomed. Opt. **18**(12), 121510 (2013).
5. L. Scolaro, R. A. McLaughlin, B. F. Kennedy, C. M. Saunders, and D. D. Sampson, "A review of optical coherence tomography in breast cancer," Photonics Lasers Med. **3**(3), 225–240 (2014).
6. X. Yao, Y. Gan, E. Chang, H. Hibshoosh, S. Feldman, and C. Hendon, "Visualization and tissue classification of human breast cancer images using ultrahigh-resolution oct," Lasers Surg. Med. **49**, 258–269 (2017).
7. S. J. Erickson-Bhatt, R. M. Nolan, N. D. Shemonski, S. G. Adie, J. Putney, D. Darga, D. T. McCormick, A. J. Cittadine, A. M. Zysk, M. Marjanovic, E. J. Chaney, G. L. Monroy, F. A. South, K. A. Cradock, Z. G. Liu, M. Sundaram, P. S. Ray, and S. A. Boppart, "Real-time imaging of the resection bed using a handheld probe to reduce incidence of microscopic positive margins in cancer surgery," Cancer Res. **75**(18), 3706–3712 (2015).
8. F. T. Nguyen, A. M. Zysk, E. J. Chaney, S. G. Adie, J. G. Kotynek, U. J. Oliphant, F. J. Bellafiore, K. M. Rowland, P. A. Johnson, and S. A. Boppart, "Optical coherence tomography: the intraoperative assessment of lymph nodes in breast cancer," IEEE Eng. Med. Biol. Mag. **29**(2), 63–70 (2010).
9. P.-L. Hsiung, D. R. Phatak, Y. Chen, A. D. Aguirre, J. G. Fujimoto, and J. L. Connolly, "Benign and malignant lesions in the human breast depicted with ultrahigh resolution and three-dimensional optical coherence tomography," Radiology **244**(3), 865–874 (2007).
10. K. S. Yemul, A. M. Zysk, A. L. Richardson, K. V. Tangella, and L. K. Jacobs, "Interpretation of optical coherence tomography images for breast tissue assessment," Surg. Innov. **26**(1), 50–56 (2019).
11. S. A. Boppart, W. Luo, D. L. Marks, and K. W. Singletary, "Optical coherence tomography: Feasibility for basic research and image-guided surgery of breast cancer," Breast Cancer Res. Treat. **84**(2), 85–97 (2004).
12. W. M. Allen, K. M. Kennedy, Q. Fang, L. Chin, A. Curatolo, L. Watts, R. Zilkens, S. L. Chin, B. F. Dessauvagie, B. Latham, C. M. Saunders, and B. F. Kennedy, "Wide-field quantitative micro-elastography of human breast tissue," Biomed. Opt. Express **9**(3), 1082–1096 (2018).
13. M. Villiger, D. Lorenser, R. A. McLaughlin, B. C. Quirk, R. W. Kirk, B. E. Bouma, and D. D. Sampson, "Deep tissue volume imaging of birefringence through fibre-optic needle probes for the delineation of breast tumour," Sci. Rep. **6**(1), 28771 (2016).
14. J. Wang, Y. Xu, K. J. Mesa, F. A. South, E. J. Chaney, J. Spillman, D. R. Barkalifa, M. Marjanovic, P. S. Carney, A. M. Higham, Z. G. Liu, and S. A. Boppart, "Complementary use of polarization-sensitive and standard OCT metrics for enhanced intraoperative differentiation of breast cancer," Biomed. Opt. Express **9**(12), 6519–6528 (2018).
15. J. Heidkamp, M. Scholte, C. Rosman, S. Manohar, J. J. Fütterer, and M. M. Rovers, "Novel imaging techniques for intraoperative margin assessment in surgical oncology: A systematic review," Int. J. Cancer **149**, 635–645 (2021).
16. J. Schwarz and H. Schmidt, "Technology for intraoperative margin assessment in breast cancer," Ann. Surg. Oncol. **27**(7), 2278–2287 (2020).
17. A. R. Pradipta, T. Tanei, K. Morimoto, K. Shimazu, S. Noguchi, and K. Tanaka, "Emerging technologies for real-time intraoperative margin assessment in future breast-conserving surgery," Adv. Sci. **7**, 1901519 (2020).
18. H. Nyquist, "Certain topics in telegraph transmission theory," Trans. Am. Inst. Electr. Eng. **47**(2), 617–644 (1928).
19. C. E. Shannon, "Communication in the presence of noise," Proc. IRE **37**(1), 10–21 (1949).
20. X. Liu and J. U. Kang, *Sparse OCT: Optimizing Compressed Sensing in Spectral Domain Optical Coherence Tomography*, vol. 7904 of *SPIE BiOS* (SPIE, 2011).
21. D. L. Donoho and M. Elad, "Optimally sparse representation in general (nonorthogonal) dictionaries via ℓ^1 minimization," Proc. Natl. Acad. Sci. U. S. A. **100**(5), 2197–2202 (2003).
22. M. Lustig, D. Donoho, and J. M. Pauly, "Sparse mri: The application of compressed sensing for rapid MR imaging," Magn. Reson. Med. **58**, 1182–1195 (2007).
23. H. Jung, J. C. Ye, and E. Y. Kim, "Improved k–t blast and k–t sense using focuss," Phys. Med. Biol. **52**(11), 3201–3226 (2007).
24. U. Gamper, P. Boesiger, and S. Kozerke, "Compressed sensing in dynamic MRI," Magn. Reson. Med. **59**, 365–373 (2008).
25. G.-H. Chen, J. Tang, and S. Leng, "Prior image constrained compressed sensing (PICCS): A method to accurately reconstruct dynamic CT images from highly undersampled projection data sets," Med. Phys. **35**(2), 660–663 (2008).
26. M. Süzen, A. Giannoula, and T. Durduran, "Compressed sensing in diffuse optical tomography," Opt. Express **18**(23), 23676–23690 (2010).

27. O. Lee, J. M. Kim, Y. Bresler, and J. C. Ye, "Compressive diffuse optical tomography: Noniterative exact reconstruction using joint sparsity," IEEE Trans. Med. Imaging **30**(1), 38–51 (2011).

28. G. Zijian, L. Changhui, S. Liang, and V. W. Lihong, "Compressed sensing in photoacoustic tomography in vivo," J. Biomed. Opt. **15**(2), 021311 (2010).

29. P. Kruizinga, P. van der Meulen, A. Fedjajevs, F. Mastik, G. Springeling, N. de Jong, J. G. Bosch, and G. Leus, "Compressive 3d ultrasound imaging using a single sensor," Sci. Adv. **3**(12), e1701423 (2017).

30. H. Lan, J. Zhang, C. Yang, and F. Gao, "Compressed sensing for photoacoustic computed tomography based on an untrained neural network with a shape prior," Biomed. Opt. Express **12**(12), 7835–7848 (2021).

31. X. Liu, S. Dai, M. Wang, and Y. Zhang, "Compressed sensing photoacoustic imaging reconstruction using elastic net approach," Mol. Imaging **2022**, 1–9 (2022).

32. X. Zhang, F. Ma, Y. Zhang, J. Wang, C. Liu, and J. Meng, "Sparse-sampling photoacoustic computed tomography: Deep learning vs. compressed sensing," Biomed. Signal Process. Control. **71**, 103233 (2022).

33. S. Schwartz, C. Liu, A. Wong, D. A. Clausi, P. Fieguth, and K. Bizheva, "Energy-guided learning approach to compressive FD-OCT," Opt. Express **21**(1), 329–344 (2013).

34. E. Lebed, P. J. Mackenzie, M. V. Sarunic, and M. F. Beg, "Rapid volumetric OCT image acquisition using compressive sampling," Opt. Express **18**(20), 21003–21012 (2010).

35. D. Xu, N. Vaswani, Y. Huang, and J. U. Kang, "Modified compressive sensing optical coherence tomography with noise reduction," Opt. Lett. **37**(20), 4209–4211 (2012).

36. W. Liao, J. Hsieh, C. Wang, W. Zhang, S. Ai, Z. Peng, Z. Chen, B. He, X. Zhang, N. Zhang, B. Tang, and P. Xue, "Compressed sensing spectral domain optical coherence tomography with a hardware sparse-sampled camera," Opt. Lett. **44**(12), 2955–2958 (2019).

37. L.-A. Duflot, A. Krupa, B. Tamadazte, and N. Andreff, "Shearlet transform: A good candidate for compressed sensing in optical coherence tomography," in *38th Annual International Conference of the IEEE Engineering in Medicine and Biology Society (EMBC)*, (IEEE, 2016).

38. J. P. McLean and C. P. Hendon, "3-d compressed sensing optical coherence tomography using predictive coding," Biomed. Opt. Express **12**(4), 2531–2549 (2021).

39. J. Yang, Y. Zhang, and W. Yin, "A fast alternating direction method for tvl1-l2 signal reconstruction from partial fourier data," IEEE J. Sel. Top. Signal Process. **4**(2), 288–297 (2010).

40. W. Zhou, A. C. Bovik, H. R. Sheikh, and E. P. Simoncelli, "Image quality assessment: from error visibility to structural similarity," IEEE Trans. on Image Process. **13**(4), 600–612 (2004).

41. H. Faragalla, B. Davoudi, N. Nofech-Moses, Y. Yucel, and K. Jakate, "The use of optical coherence tomography for gross examination and sampling of fixed breast specimens: A pilot study," Diagnostics **12**(9), 2191 (2022).

42. Y. Gan, X. Yao, E. Chang, S. B. Amir, H. Hibshoosh, S. Feldman, and C. P. Hendon, "Comparative study of texture features in OCT images at different scales for human breast tissue classification," in *38th Annual International Conference of the IEEE Engineering in Medicine and Biology Society (EMBC)*, (IEEE, 2016).

43. J. Ding, X. H. Hu, and V. Gudivada, "A machine learning based framework for verification and validation of massive scale image data," IEEE Trans. Big Data **7**(2), 451–467 (2021).

44. C. Xia, K. Niu, Z. He, S. Tang, J. Wang, Y. Zhang, Z. Zhao, and W. Guo, "SVM-based bone tumor detection by using the texture features of x-ray image," in *2018 International Conference on Network Infrastructure and Digital Content (IC-NIDC)*, (2018), pp. 130–134.

45. Y. Ling, Z. Dong, X. Li, Y. Gan, and Y. Su, "Deep learning empowered highly compressive SS-OCT via learnable spectral–spatial sub-sampling," Opt. Lett. **48**(7), 1910 (2023).

46. A. K. Venkataramanan, C. Wu, A. C. Bovik, I. Katsavounidis, and Z. Shahid, "A hitchhiker's guide to structural similarity," IEEE Access **9**, 28872–28896 (2021).